MIT Libraries | DSpace@MIT

MIT Open Access Articles

3D nanofabrication by volumetric deposition and controlled shrinkage of patterned scaffolds

Massachusetts Institute of Technology

3-D Nanofabrication by Volumetric Deposition and Controlled Shrinkage of Patterned Scaffolds

Daniel Oran[1,†], **Samuel G. Rodriques**[1,2,†], **Ruixuan Gao**[1], **Shoh Asano**[1,3], **Mark A. Skylar-Scott**[4,5], **Fei Chen**[1,6], **Paul W. Tillberg**[1,7,11], **Adam H. Marblestone**[#1,††], and **Edward S. Boyden**[#1,6,8,9,10,*,††]

[1]MIT Media Lab, Massachusetts Institute of Technology, Cambridge, MA 02139

[2]Department of Physics, Massachusetts Institute of Technology, Cambridge, MA 02139

[3]Pfizer Internal Medicine Research Unit, Cambridge, Massachusetts, 02139

[4]Harvard John A. Paulson School of Engineering and Applied Sciences, Harvard University, Cambridge, MA 02138

[5]Wyss Institute for Biologically Inspired Engineering, Cambridge, MA 02138

[6]Department of Biological Engineering, Massachusetts Institute of Technology, Cambridge, MA 02139

[7]Department of Electrical Engineering and Computer Science, Massachusetts Institute of Technology, Cambridge, MA 02139

[8]Department of Brain and Cognitive Sciences, Massachusetts Institute of Technology, Cambridge, MA 02139

[9]MIT McGovern Institute, Massachusetts Institute of Technology, Cambridge, MA 02139

[10]Koch Institute, Massachusetts Institute of Technology, Cambridge, MA 02139

[11]Present address: Janelia Research Campus, Ashburn, VA, 20147

[#] These authors contributed equally to this work.

[*]Correspondence to: esb@media.mit.edu.
[†]These authors contributed equally to this work.
[††]These authors contributed equally to this work.

Abstract

Lithographic nanofabrication is often limited to successive fabrication of two-dimensional layers. We present a strategy for the direct assembly of three-dimensional nanomaterials consisting of metals, semiconductors, and biomolecules arranged in virtually any three-dimensional geometry. We use hydrogels as scaffolds for volumetric deposition of materials at defined points in space. We then optically pattern these scaffolds in three dimensions, attach one or more functional materials, and then shrink and dehydrate them in a controlled way to achieve nanoscale feature sizes in a solid substrate. We demonstrate this process, Implosion Fabrication (ImpFab), by directly writing highly conductive, 3D silver nanostructures within an acrylic scaffold using a volumetric silver deposition process, achieving resolutions in the tens of nanometers and complex, non-self-supporting 3D geometries of interest for optical metamaterials.

One Sentence Summary:

We demonstrate direct writing of nanoscale 3D structures of metals and semiconductors with no limitations on geometry.

Most nanofabrication techniques currently rely on 2- and 2.5-dimensional patterning strategies. Although popular direct laser writing methods allow for the single-step fabrication of self-supporting, polymeric 3D nanostructures (1–8), arbitrary 3-D nanostructures (e.g., solid spheres of metal, or metallic wires arranged in discontinuous patterns) are not possible (9, 10). This raises the question of whether a versatile 3D nanofabrication strategy could be developed that would allow independent control over the geometry, feature size, and chemical composition of the final material.

A hallmark of 2D nanofabrication strategies is that materials are deposited in a planar fashion onto a patterned surface. By analogy, we reasoned that a general 3D nanofabrication strategy could involve deposition of materials in a volumetric fashion into a patterned scaffold. However, such scaffolds face a fundamental tension: they should be porous and solvated, to allow for introduction of reagents to their interior, while also being dense, to allow material placement with nanoscale precision. To resolve this contradiction, we reasoned that an ideal scaffold could be patterned in a solvated state, and then collapsed and desiccated in a controlled way, densifying the patterned materials to obtain nanoscale feature sizes. Although several groups have previously experimented with shrinking materials, the shrinking process typically requires harsh conditions and chemical changes that may destroy functional materials (11–13). We use polyacrylate/polyacrylamide hydrogels for the scaffold material, as they have pore sizes in the range of 10nm to 100nm (14), are known for their ability to expand and shrink up to ~10-fold in linear dimension (15–18), and methods for optically patterning hydrogels are well-established (19–23).

Our implementation takes place in three phases (24). It has previously been found that two-photon excitation of fluorescein within acrylate hydrogels causes the fluorescein to react to the hydrogel (21–23). We take advantage of this phenomenon to attach fluorescein molecules carrying reactive groups to the expanded gel in defined three-dimensional patterns (Fig. 1A,B). In the second phase, following removal of the fluorescein patterning solution, the gel is functionalized by depositing materials onto the patterned reactive groups (Fig.

1C,D), using one of several available conjugation chemistries. This volumetric deposition step defines the composition of the material, and may be followed by additional deposition chemistries ("intensification") to boost the functionality of the deposited molecules or nanomaterials (Fig. 1E,F). Importantly, the functional molecules or nanoparticles are not present during the patterning process, so the specific physical properties of the molecules or nanoparticles used will not affect the patterning. In the final phase, the patterned and functionalized scaffold is shrunken by a factor of 10 to 20 in each dimension with acid or divalent cations over a period of hours, and dehydrated to achieve the desired nanoscale resolution (Fig. 1G,H). The scaffold is not removed, as it supports the nanofabricated material and allows for the creation of disconnected or high-aspect-ratio structures that would otherwise collapse outside of the gel.

We found the polyacrylate gel to be a suitable substrate for patterning and deposition. The gel readily accommodates a wide variety of hydrophilic reagents, including small molecules, biomolecules, semiconductor nanoparticles or metal nanoparticles (S1A-C). For laser powers below a critical threshold, the density of the deposited functional material is controllable (Fig. 1I, S2). We estimated based on the maximum pattern fluorescence in Fig. S2A that binding sites are patterned into the gel at concentrations of at least 79.2μM in the expanded state, leading to a final concentration in the shrunken state of greater than 272.0mM or 1.64×10^{20} sites per cubic centimeter for a 10x gel (see below). By repeating our patterning and deposition process, we were able to deposit multiple materials in different patterns in the same substrate, such as gold nanoparticles and cadmium telluride nanoparticles (Fig. 1J). We observed by fluorescence that the deposition of the second material onto the first pattern was at most 18.5% of the deposition of the second material onto the second pattern, confirming that multiple materials may be independently patterned and deposited using this process (Fig. S3).

The shrinking process is performed either by exposing the expanded gel to hydrochloric acid or to divalent cations (e.g. magnesium chloride, Fig. S1A-C). The latter may be useful if the patterned materials are sensitive to acid, although we found that both streptavidin and DNA remain functionally intact following acid shrinking (Fig. S1D). Gels that are shrunken in hydrochloric acid can subsequently be dehydrated, resulting in additional shrinking, and this process preserves the patterned geometry (Fig. 1K). The final dehydrated gel is transparent (Fig. S4A), and atomic force microscopy (AFM) characterization measured the surface roughness over a 1×1 μm^2 window to be ~0.19 nm (root-mean square; Fig. S4B). Except where stated otherwise, all samples described as "shrunken" hereafter are shrunken and dehydrated. We tested two different gel formulations that differ only in cross-linker concentration: "10x" (0.075% cross-linker) and "20x" (0.0172% cross-linker) (24). The 10x gels, and the patterns within, shrink consistently by a linear factor of 10.6 ± 0.8 in the lateral dimension (mean ± s.d., n=5 gels) and 34.8 ± 1.8 in the axial dimension (n=6 gels, Fig. 1L), with the disproportionate axial shrink occurring during dehydration, possibly due to surface interactions between the shrinking polymer and the surface of the glass container. For the 20x gels, we observed 20.1 ± 2.9-fold shrink in the lateral dimension (n=4 gels, Fig. 1M). The 20x gel formulation is challenging to handle manually due to its delicacy, so the axial shrink factor was not measured, and they were not used further, except for distortion measurements.

To validate the minimum feature size of ImpFab, we designed a test pattern containing pairs of single-voxel-wide lines (Fig. 2A-D). Since such post-shrink features are necessarily below the optical diffraction limit, we deposited gold nanoparticles and employed scanning electron microscopy (SEM) to assess the resolution after shrinking. We estimated the resolution by measuring the line width (full width at half maximum, FWHM) (Fig. 2E-G), and obtained a value of 59.6 ± 3.8 nm (mean $\pm$ s.d. across samples; n = 5; Fig. 2H) for 10x gels. The mean within-sample standard deviation of the line width was 8.3 nm. We estimated the isotropy of the shrinking process by calculating the ratio of the longest diameter of the patterned circle to the orthogonal diameter (Fig. 2C, D). The percent distortion thus calculated was $6.8 \pm 6.9\%$ for 10x gels (mean $\pm$ s.d., n=6 gels), and $8.2 \pm 4.3\%$ for 20x gels (n=4 gels). We found that the ratio of axial to lateral shrink was on average within $3.1 \pm 2.5\%$ of the mean of this ratio (n=6 10x gels), indicating that the disproportionate axial shrink is highly reproducible. Thus, it is possible to account for the disproportionate axial shrink in the design of the pattern. To illustrate this point with the fabrication of a cube, we patterned a rectangular prism and imaged it before and after dehydration (Fig. S5). As expected, the rectangular prism contracts in the axial dimension during the dehydration step and turns into a cube.

Since nanoscale metal structures are broadly important in fields such as nanophotonics, metamaterials, and plasmonics, we applied ImpFab to create conductive silver structures. We anchored gold nanoparticles to patterned amines via a biotin-streptavidin linkage (24). We were initially unable to deposit gold nanoparticles at high enough concentrations to form conductive structures. We thus developed an intensification process based on photographic intensification chemistries, in which silver is deposited onto the surface of gel-anchored gold nanoparticles in aqueous phase while the gel is in the expanded state (Fig. 1E, F). Finally, the gel is treated with a chelating agent to remove any remaining dissolved silver, and is then shrunken via exposure to hydrochloric acid and subsequent dehydration.

Even with the silver intensification process, wire structures fabricated using the method above (Fig. 3A) were not reliably conductive, or had resistances on the order of hundreds of ohms. We tested several different methods of sintering, including treatment with oxygen plasma, electrical discharge, and heating the sample to ~500 degrees in an oven. However, none of these methods resulted in well-preserved and evenly sintered silver structures. Instead, we found that the silver patterns could be sintered effectively using the same 2-photon setup used for the initial photopatterning step. We found that samples irradiated at relatively low power levels (24) showed a distinct change in the morphology of the embedded silver nanoparticles consistent with sintering (Fig. 3B,C). We measured the conductivity of three patterned silver squares both before and after sintering, and found that the resistance of each square decreased by 20–200 fold (Fig. 3D). Sintered wires were measured in a 4-point probe system, and were found to have linear IV curves (Fig. S6A). Wires sintered in this way had an average resistance of $2.85 \pm 1.68\Omega$ (mean $\pm$ standard deviation; n = 10), with the resistance depending on the density of the patterned silver (Fig. S6B). By contrast, an ideal silver wire with the same geometry would have a resistance of 0.38Ω, suggesting that our sintered structures achieved a mean conductivity 13.3% that of bulk silver, with individual samples obtaining conductivities as high as 30% that of bulk silver (Fig. 3E).

To verify that our method is compatible with a wide range of 3D geometries, we fabricated structures with dimensions ranging from hundreds of nanometers to several microns (Fig. 4A-C). We found that these structures retain their morphology following sintering (Fig. 4B). We fabricated a non-layered, non-connected three-dimensional structure comprised of many 2D substructures arranged at different angles relative to each other in space, which would not lend itself to fabrication by other means (Fig. 4D). Whereas our previous experiments had only observed the fabrication of two-dimensional silver structures, we used confocal reflection microscopy to confirm that silver was deposited throughout the volume of the 3D pattern (Fig. 4E). Finally, using confocal microscopy, we were able to validate that the structure retained its shape following shrinking (Fig. 4F).

Due to the modular nature of ImpFab, the extension of the ImpFab strategy to other kinds of materials, such as other semiconductors or metals, only requires the development of an aqueous deposition chemistry that is compatible with the gel substrate. Future iterations may use alternative chemistries, such as dendrimeric complexes for direct deposition of metals or semiconductors within the hydrogel (25, 26), or DNA-addressed material deposition (27). Finally, we note that although we used a conventional microscope that is not optimized for patterning, and that was limited to a 4cm/s scan speed (in post-shrink dimensions), we were able to create objects spanning hundreds of microns to millimeters (Fig. S7). Using faster patterning systems (23), ImpFab could ultimately enable the creation of centimeter-scale nanomaterials.

Supplementary Material

Refer to Web version on PubMed Central for supplementary material.

Acknowledgements

References and Notes:

1. Deubel M et al., Direct laser writing of three-dimensional photonic-crystal templates for telecommunications. Nat. Mater 3, 444–447 (2004). [PubMed: 15195083]

2. Soukoulis CM, Wegener M, Past achievements and future challenges in the development of three-dimensional photonic metamaterials. Nat. Photonics 5, 523–530 (2011).

3. Ross CA, Berggren KK, Cheng JY, Jung YS, Chang J-B, Three-Dimensional Nanofabrication by Block Copolymer Self-Assembly. Adv. Mater 26, 4386–4396 (2014). [PubMed: 24706521]

4. Chang J-B et al., Design rules for self-assembled block copolymer patterns using tiled templates. Nat. Commun 5, 3305 (2014). [PubMed: 24531135]

5. Wathuthanthri I, Liu Y, Du K, Xu W, Choi C-H, Simple Holographic Patterning for High-Aspect-Ratio Three-Dimensional Nanostructures with Large Coverage Area. Adv. Funct. Mater 23, 608–618 (2013).

6. Matsui S, Kaito T, Fujita J, Komuro M, Kanda K, Three-dimensional nanostructure fabrication by focused-ion-beam chemical vapor deposition Three-dimensional nanostructure fabrication by focused-ion-beam chemical vapor deposition. J. Vac. Sci. Technol. B Microelectron. Nanom. Struct. Process. Meas. Phenom 3181, 3–7 (2013).

7. Kawata S, Sun HB, Tanaka T, Takada K, Finer features for functional microdevices. Nature 412, 697–698 (2001). [PubMed: 11507627]

8. Meza LR, Das S, Greer JR, Strong, lightweight, and recoverable three-dimensional ceramic nanolattices. Science 345, 1322–6 (2014). [PubMed: 25214624]

9. Vyatskikh A et al., Additive manufacturing of 3D nano-architected metals. Nat. Commun 9, 593 (2018). [PubMed: 29426947]

10. Cao YY, Takeyasu N, Tanaka T, Duan XM, Kawata S, 3D metallic nanostructure fabrication by surfactant-assisted multiphoton-induced reduction. Small 5, 1144–1148 (2009). [PubMed: 19291732]

11. Bauer J, Schroer A, Schwaiger R, Kraft O, Approaching theoretical strength in glassy carbon nanolattices. Nat. Mater 15, 438–443 (2016). [PubMed: 26828314]

12. Hegde M et al., 3D Printing All-Aromatic Polyimides using Mask-Projection Stereolithography: Processing the Nonprocessable. Adv. Mater 29, 1701240 (2017).

13. Zhao X-M, Xia Y, Schueller OJA, Qin D, Whitesides GM, Fabrication of microstructures using shrinkable polystyrene films. Sensors Actuators A Phys 65, 209–217 (1998).

14. Holmes DL, Stellwagen NC, Estimation of polyacrylamide gel pore size from Ferguson plots of linear DNA fragments. II. Comparison of gels with different crosslinker concentrations, added agarose and added linear polyacrylamide. Electrophoresis 12, 612–619 (1991). [PubMed: 1752240]

15. Chen F, Tillberg PW, Boyden ES, Expansion microscopy. Science 347, 543–8 (2015). [PubMed: 25592419]

16. Ilmain F, Tanaka T, Kokufuta E, Volume transition in a gel driven by hydrogen bonding. Nature 349, 400–401 (1991).

17. Hirokawa Y, Tanaka T, in AIP Conference Proceedings (American Institute of Physics, 1984; http://aip.scitation.org/doi/abs/10.1063/1.34300), vol. 107, pp. 203–208.

18. Suzuki A, Tanaka T, Phase transition in polymer gels induced by visible light. Nature 346, 345–347 (1990).

19. DeForest CA, Anseth KS, Cytocompatible click-based hydrogels with dynamically tunable properties through orthogonal photoconjugation and photocleavage reactions. Nat. Chem 3, 925–931 (2011). [PubMed: 22109271]

20. DeForest CA, Anseth KS, Photoreversible Patterning of Biomolecules within Click-Based Hydrogels. Angew. Chemie 124, 1852–1855 (2012).

21. Skylar-Scott MA, Liu M-C, Wu Y, Yanik MF, von Freymann G, Schoenfeld WV, Rumpf RC, Eds. (International Society for Optics and Photonics, 2017), vol. 10115, p. 101150L.

22. Skylar-Scott MA, Liu M-C, Wu Y, Dixit A, Yanik MF, Guided Homing of Cells in Multi-Photon Microfabricated Bioscaffolds. Adv. Healthc. Mater 5, 1233–1243 (2016). [PubMed: 27059425]

23. Scott MA, Wissner-Gross ZD, Yanik MF, Ultra-rapid laser protein micropatterning: screening for directed polarization of single neurons. Lab Chip 12, 2265 (2012). [PubMed: 22596091]

24. Materials and methods are available as supplementary materials online.

25. Miura A et al., Fabrication of gold clusters photoreduced in gold-dendrimer complex nanoparticles. Opt. Mater. Express 7 (2017), doi:10.1364/OME.7.002224.

26. Esumi K, Suzuki A, Aihara N, Usui K, Torigoe K, Preparation of Gold Colloids with UV Irradiation Using Dendrimers as Stabilizer. Langmuir 14, 3157–3159 (1998).

27. Rothemund PWK, Folding DNA to create nanoscale shapes and patterns. Nature 440, 297–302 (2006). [PubMed: 16541064]

28. Burckel DB et al., Micrometer-Scale Cubic Unit Cell 3D Metamaterial Layers. Adv. Mater 22, 5053–5057 (2010). [PubMed: 20941794]
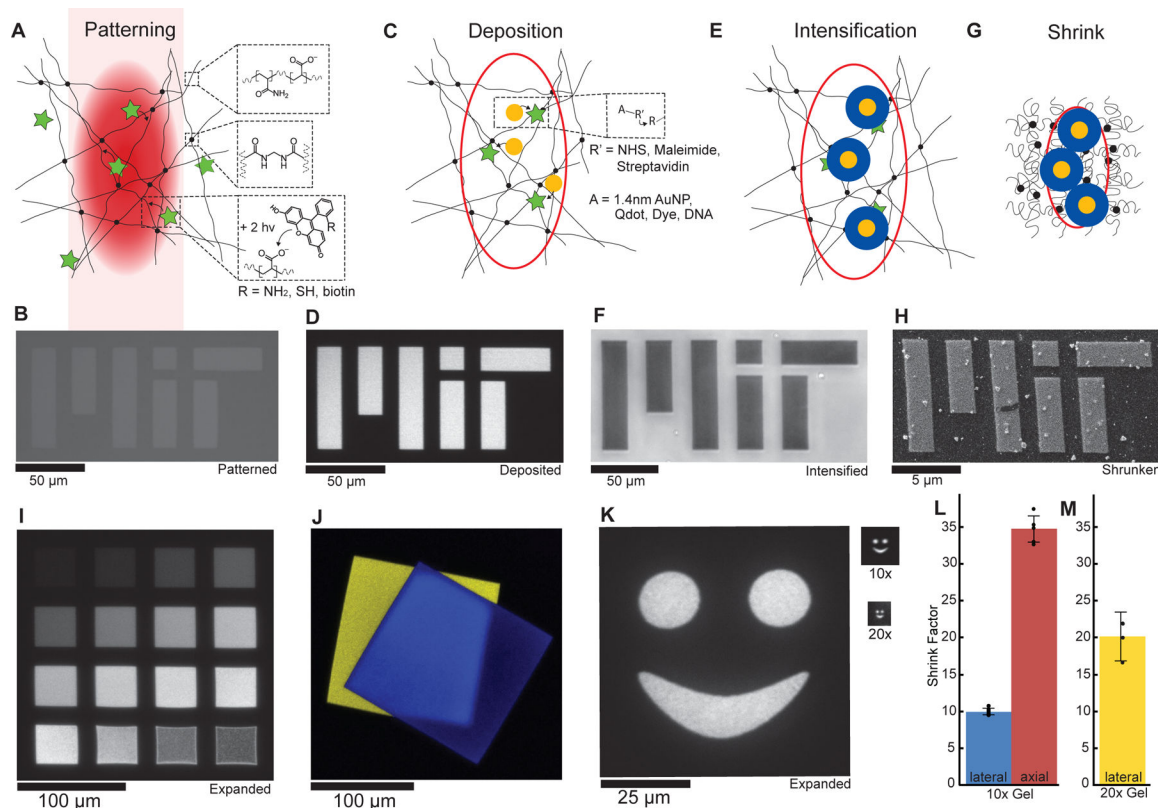
Fig. 1.

Implosion fabrication (ImpFab) process. (**A**) Schematic of the patterning process, showing the expanded polyelectrolyte gel (black lines and dots, top insets), and fluorescein (green star, bottom inset) binding covalently to the polymer matrix upon multi-photon excitation (red volume). Not to scale. Fluorescein bears a reactive group, R. (**B**) Residual fluorescence of patterned fluorescein immediately following patterning. (**C**) Schematic of functionalization of patterned gel by attaching small molecules, proteins, DNA or nanoparticles to reactive R groups from (A). Red outline indicates patterned volume in (A). (**D**) Image of fluorescent streptavidin nanogold conjugates attached to the pattern in (B). (**E**) Schematic of the volumetric deposition process, showing growth of silver (blue) on top of gold nanoparticles within the hydrogel matrix. (**F**) Image of silver deposited onto the pattern in (D) by transmission optical microscopy. Following silver growth, the pattern has high optical density. (**G**) Schematic of the shrinking and dehydration process. (**H**) SEM image of the silverized pattern from (F) following shrinking and dehydration. (**I**) Fluorescent patterns created with different laser powers(24). (**J**) Image of a gel patterned with both metal nanoparticles (yellow) and CdTe quantum dots (blue) in different locations. (**K**) Images of fluorescent patterns before shrinking (left, 10x gel), after shrinking and dehydration in a 10x gel (top right), and after shrinking and dehydration in a 20x gel (bottom right). (**L**) The mean lateral (blue) and axial (red) shrink factors (initial size/final size) for 10x gels (n = 6), including dehydration. (**M**) The mean lateral shrink factor for 20x gels (yellow, n = 3). Error bars show s.d.
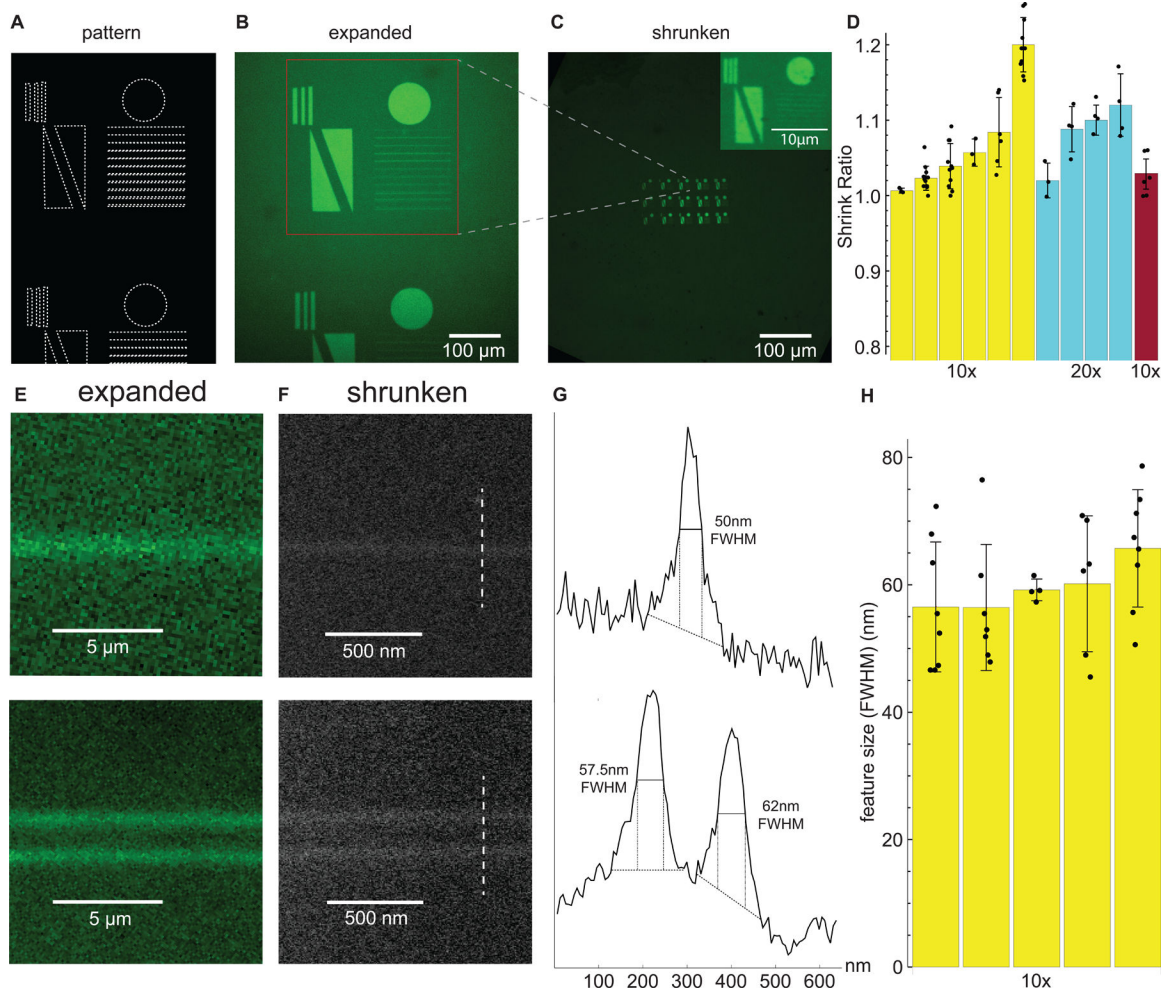
Fig. 2.

Resolution of implosion fabrication. (A) Design of the resolution test pattern including pairs of single-voxel-thick lines (bottom right). (B) Fluorescence image of the patterns from (A). (C) Fluorescence image of the pattern (from B) after shrinking. (D) Measures of isotropy in lateral and axial dimensions. Yellow and blue bars represent lateral isotropy for 10x gels and 20x gels, respectively, and the red bar represents axial isotropy for 10x gels. (E) Fluorescence images of single-voxel lines before shrinking. (F) Scanning electron microscopy (SEM) images of single-voxel lines after 10x shrinking. The gel was functionalized with gold nanoparticles for contrast. (G) Cross-sectional intensity profiles of the lines imaged by SEM (dashed lines in (F)), showing how full-width half-maxima (FWHM) of single voxel lines were measured. (H) Linewidths, measured in G, for five different gel samples. Dots are measurements for individual lines; bars indicate mean ± s.d. across individual lines within a single gel.
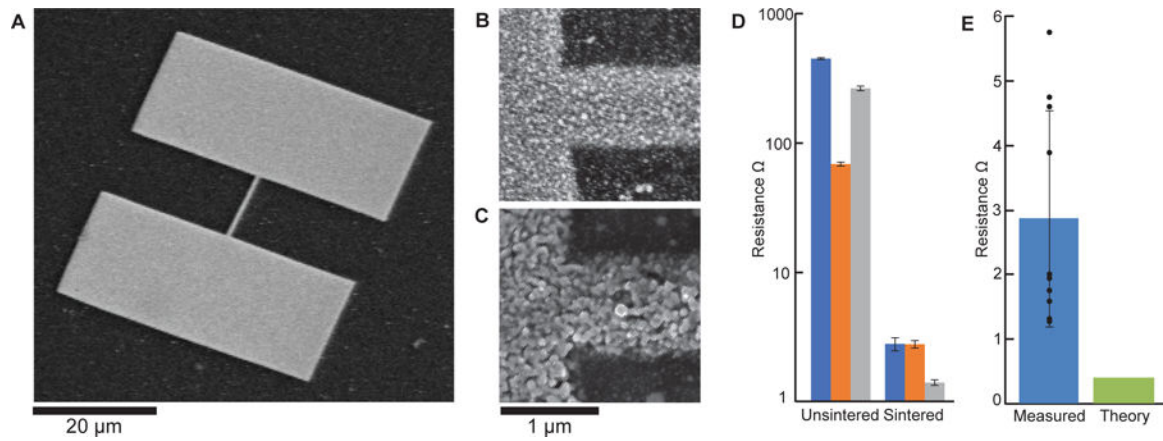
Fig. 3.
Characterization of silver conductivity. (A) SEM overview of a shrunken silver wire between two landing pads, prior to sintering. (B) SEM image of wires before and (C) after sintering. (D) Resistance of three separate conductive pads, of dimension 35×35 μm, measured before and after sintering. Each color represents a single conductive pad. Error bars show standard error in a four-point conductivity measurement. (E) Resistance of individual sintered wires (black dots), their mean (blue), and standard deviation, as compared to the theoretical conductivity of a similar structure made of bulk silver (green).
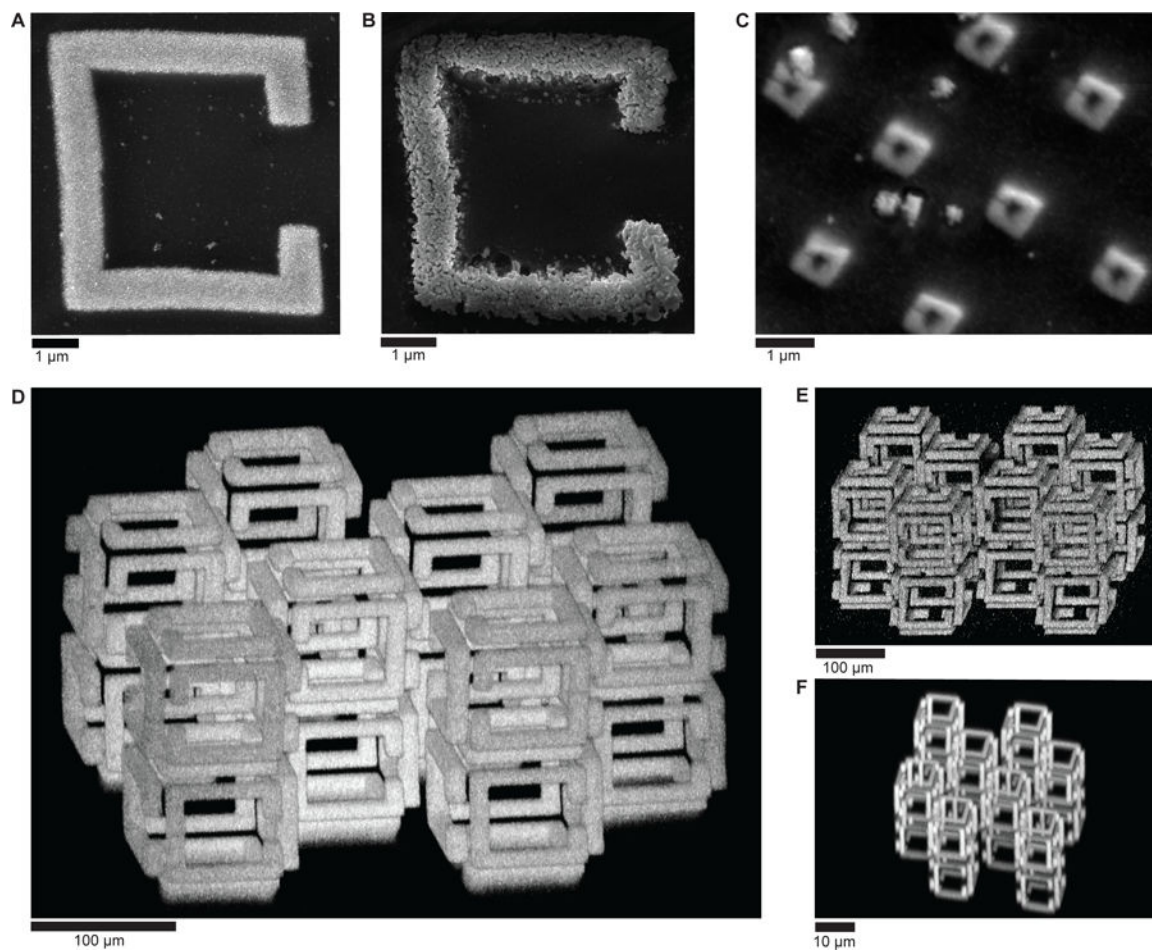
Fig 4.
Fabrication of 3D metal nanostructures. (A) Two-dimensional structures fabricated with ImpFab with micron-scale resolution, before and (B) after sintering, visualized using SEM. (C) Similar structures fabricated with hundred-nanometer feature size, after shrinking and dehydration but before sintering. (D) Maximum intensity projection of fluorescence image of a 3D structure prior to shrinking (2, 28). (E) Maximum intensity projection of a reflected light image from the same structure following volumetric silver deposition, prior to shrinking. (F) Maximum intensity projection of a fluorescence image of the same structure, shrunken but not dehydrated.